

Variational Dense Motion Estimation Using the Helmholtz Decomposition

Timo Kohlberger¹, Étienne Mémin², and Christoph Schnörr³

¹ Computer Vision, Graphics and Pattern Recognition Group
Department of Mathematics and Computer Science
University of Mannheim, 68131 Mannheim, Germany
`{tiko,schnoerr}@uni-mannheim.de`

² IRISA/Université de Rennes I
Campus universitaire de Beaulieu
35042 Rennes, Cedex, France
`Etienne.Memin@irisa.fr`

Abstract. We present a novel variational approach to dense motion estimation of highly non-rigid structures in image sequences. Our representation of the motion vector field is based on the extended Helmholtz Decomposition into its principal constituents: The laminar flow and two potential functions related to the solenoidal and irrotational flow, respectively. The potential functions, which are of primary interest for flow pattern analysis in numerous application fields like remote sensing or fluid mechanics, are *directly* estimated from image sequences with a variational approach. We use regularizers with derivatives up to third order to obtain unbiased high-quality solutions. Computationally, the approach is made tractable by means of auxiliary variables. The performance of the approach is demonstrated with ground-truth experiments and real-world data.

1 Introduction

In a number of domains affecting our everyday life, the analysis of image sequences involving fluid phenomena is of importance. This includes for instance domains such as visualization in experimental fluid mechanics [1,12], environmental sciences (meteorology [3,4,11,13,21], oceanography [6]) or medical imaging [2,7,18]. For all these domains it is of primary interest to extract reliable velocity fields and to the observed fluid flow. With respect to that goal, image sensors have considerable advantages compared to dedicated probes. Compared to these probes, image sensors provide a huge amount of almost continuous spatio-temporal data in a fast, tireless, reproducible and contact-free way. However, the sought motion information has then to be extracted from the luminance function which is not an easy task.

But in such a fluid context the extraction of a velocity field is far from being the ultimate goal of the analysis. Differential or integrated information from the velocity field is indeed far more valuable for concerned experts. For example, it

is essential to characterize fluid flows to extract the vorticity fields, the streamlines, or the singular points of the flows. All these features may be estimated indirectly from the velocity field by differentiation or by integration. Among all these information, the two potential functions called the *velocity potential* and the *stream function* are of great interest: (i) their gradients provide a description of the *irrotational* and the *solenoidal* components of the velocity fields; (ii) their Laplacians give access to the *vorticity* and the *divergence* of the velocity fields; (iii) their level lines allow us to extract directly the streamlines and the equipotential curves of the velocity potentials; (iv) their extrema provide the location of the singular points of major interest [5] (namely *sources*, *sinks* and *vortexes*).

Knowing the curl and the divergence of the flow, the extraction of such potential functions can be done by solving two Dirichlet problems. Such an estimation is particularly difficult for sparse velocity fields such as those obtained by the usual correlation methods [12] since an additional interpolation step is needed [16,17]. Dense motion estimation, on the other hand, allows to recover these potential functions more accurately. However, such an estimation as proposed in [5] is not “direct”. It requires a process of three steps: First, the motion field has to be extracted, next the motion field is separated into its irrotational and solenoidal components, and finally the potential functions are estimated from these two vector fields by integration.

In this paper, we propose to estimate directly the *velocity potential* and the *stream function* from the luminance data. Instead of expressing the velocity field explicitly, it is represented by its *irrotational*, *solenoidal* and *laminar* components using the Helmholtz decomposition with a non-zero border condition. In addition, the first two components are expressed explicitly by the *velocity potential* and the *stream function*. This representation is applied to the Brightness Constancy Constraint Equation (BCCE) and embedded into an energy functional using a quadratic penalizer function. In a second step a structure preserving regularization based on the divergence of the *velocity potential* and the curl of the *stream function* is introduced. Since the original regularization contains high-order derivatives causing numerical difficulties it is then modified by introducing auxiliary variables. Finally the energy is integrated in a multi-resolution framework to minimize linearization errors.

The second section of this paper describes the representation of the decomposed velocity field and its integration into the BCCE. Furthermore, the regularization is introduced and the embedding into a multi-resolution framework as well as the energy minimization is described. The third section is dedicated to three experiments. The first one illustrates the influence of regularization parameters on the approximation quality. The second experiment compares the new approach to the approach of Corpetti et al. [5] by means of two dedicated cases. In the third and last experiment the approach is applied to real data. Finally, we conclude with a discussion in section four.

2 Description of the Approach

2.1 Helmholtz Decomposition and BCCE

Let us consider a smooth vector field $\mathbf{w} = (u(x, y), v(x, y))^{\top} : \mathbb{R}^2 \rightarrow \mathbb{R}^2$ defined over a section Ω of the image plane. Without loss of generality we can extend \mathbf{w} to the whole plane and assume that it vanishes at infinity. As a consequence, it can be decomposed into a sum of a divergence free component (marked as *solenoidal*) and a curl free component (marked as *irrotational*). This decomposition is known as the *Helmholtz Decomposition* of a vector field

$$\mathbf{w} = \mathbf{w}_{so} + \mathbf{w}_{ir} \quad (1)$$

with

$$\operatorname{div} \mathbf{w}_{so} = \frac{\partial u}{\partial x} + \frac{\partial v}{\partial y} = 0 \quad \text{and} \quad \operatorname{curl} \mathbf{w}_{ir} = -\frac{\partial v}{\partial x} + \frac{\partial u}{\partial y} = 0. \quad (2)$$

In case of a non-zero border condition, the decomposition also includes a *laminar* component which is both irrotational and solenoidal:

$$\mathbf{w} = \mathbf{w}_{so} + \mathbf{w}_{ir} + \mathbf{w}_{lam}. \quad (3)$$

Furthermore, it is well known that both \mathbf{w}_{so} and \mathbf{w}_{ir} derive from potential functions ϕ and $\psi : \Omega \rightarrow \mathbb{R}$ denoted as *stream potential* and *velocity potential*, respectively:

$$\mathbf{w}_{ir} = \nabla \phi = \left(\frac{\partial \phi}{\partial x}, \frac{\partial \phi}{\partial y} \right)^{\top} \quad (4)$$

$$\mathbf{w}_{so} = \nabla \psi^{\perp} = \left(-\frac{\partial \psi}{\partial y}, \frac{\partial \psi}{\partial x} \right)^{\top}. \quad (5)$$

Let \mathbf{w} denote the motion field of an image sequence $I : \Omega \times [0, T] \rightarrow \mathbb{R}$. Assuming brightness constancy, i.e. changes in intensity are due to motion only, leads to

$$I(\mathbf{x} + \mathbf{w}(\mathbf{x}, t), t + \Delta t) - I(\mathbf{x}, t) = 0 \quad (6)$$

with

$$\mathbf{w} = \nabla \phi + \nabla \psi^{\perp} + \mathbf{w}_{lam}. \quad (7)$$

The goal of the approach presented in the following paragraphs will be the *direct* approximation of those two potential fields ϕ and ψ from the brightness constancy constraint equation (6) in contrast to estimating the flow field first and followed by a path integration as proposed in [5].

The laminar component will not be of interest here. It is assumed that the motion in the given image sequence has no laminar component, which can be reached by approximating it separately in advance and removing it from the image sequence by defining $I(\mathbf{x}, t) := \bar{I}(\mathbf{x} + \mathbf{w}_{lam}(\mathbf{x}, t), t)$, with \bar{I} representing

the original sequence. In most applications \mathbf{w}_{lam} can be estimated roughly by a multi-scale Horn and Schunck estimator using a strong regularization.

Embedding (6) into an energy framework leads to the functional

$$J(\phi, \psi) := \int_{\Omega} [I(\mathbf{x} + \nabla\phi(\mathbf{x}, t) + \nabla\psi^\perp(\mathbf{x}, t), t + \Delta t) - I(\mathbf{x}, t)]^2 d\mathbf{x}, \tag{8}$$

for which optimal estimates $\hat{\phi}$ and $\hat{\psi}$ of both potentials are given by

$$(\hat{\phi}, \hat{\psi}) = \arg \min_{\phi, \psi} J(\phi, \psi) \tag{9}$$

and the corresponding flow by $\hat{\mathbf{w}} = \nabla\hat{\phi} + \nabla\hat{\psi}^\perp$, respectively. Separate linearizations for $\nabla\psi^\perp$ and $\nabla\phi$

$$J_1(\phi, \psi) := \int_{\Omega} [\nabla I(\mathbf{x} + \nabla\phi, t + \Delta t)^\top \nabla\psi^\perp + I(\mathbf{x} + \nabla\phi, t + \Delta t) - I(\mathbf{x}, t)]^2 d\mathbf{x} \tag{10}$$

$$J_2(\phi, \psi) := \int_{\Omega} [\nabla I(\mathbf{x} + \nabla\psi^\perp, t + \Delta t)^\top \nabla\phi + I(\mathbf{x} + \nabla\psi^\perp, t + \Delta t) - I(\mathbf{x}, t)]^2 d\mathbf{x} \tag{11}$$

lead to two coupled minimization problems

$$\begin{cases} \arg \min_{\psi} J_1(\phi, \psi) \\ \arg \min_{\phi} J_2(\phi, \psi) \end{cases}. \tag{12}$$

By defining abbreviations

$$\nabla I_\nu(\mathbf{x}) := \nabla I(\mathbf{x} + \nabla\nu, t + \Delta t) \tag{13}$$

$$\partial I_\nu := I(\mathbf{x} + \nabla\nu, t + \Delta t) - I(\mathbf{x}, t) \tag{14}$$

(12) can be written as

$$\begin{cases} \arg \min_{\psi} \int_{\Omega} [\nabla I_\phi^\top \nabla\psi^\perp + \partial I_\phi]^2 d\mathbf{x} \\ \arg \min_{\phi} \int_{\Omega} [\nabla I_\psi^\top \nabla\phi + \partial I_\psi]^2 d\mathbf{x}. \end{cases} \tag{15}$$

Minimizing each energy J_1, J_2 requires the first variations to vanish, i.e.

$$\left. \frac{dJ_1(\phi, \psi + \tau\tilde{\psi})}{dt} \right|_{\tau=0} = 0 \quad \text{and} \quad \left. \frac{dJ_2(\phi + \tau\tilde{\phi}, \psi)}{dt} \right|_{\tau=0} = 0, \tag{16}$$

for arbitrary test functions $\tilde{\psi}$ and $\tilde{\phi}$. This results in the system of equations:

$$\begin{cases} \int_{\Omega} \left[(\nabla I_{\phi} \nabla I_{\phi}^{\top}) \nabla \psi^{\perp} + \partial I_{\phi} \nabla I_{\phi} \right] \nabla \tilde{\psi}^{\perp} \, d\mathbf{x} = 0 \\ \int_{\Omega} \left[(\nabla I_{\psi} \nabla I_{\psi}^{\top}) \nabla \phi + \partial I_{\psi} \nabla I_{\psi} \right] \nabla \tilde{\phi} \, d\mathbf{x} = 0 \end{cases} \quad (17)$$

Since the matrices $\nabla I_{\phi} \nabla I_{\phi}^{\top}$ and $\nabla I_{\psi} \nabla I_{\psi}^{\top}$ are singular, terms of the form ϵI for small ϵ can be added to make the system well-posed. Numerical experiments revealed, however, that this regularization is too weak and does not yield satisfying results. Accordingly, we investigated additional regularizing smoothness terms which preserve the flow field structure as much as possible (see next section).

2.2 Structure-Preserving Regularization

Since the components of the motion fields (sources, sinks and vortexes) which we want to estimate explicitly in terms of potential functions ϕ and ψ contain discontinuities by their nature, first-order smoothness terms like those of the Horn and Schunck approach [9] or non-quadratic extensions [14,15,20] are inadequate. Instead we suggest using a second-order div-curl regularizer as proposed by Suter [19]:

$$\int_{\Omega} \|\nabla \operatorname{div} \mathbf{w}\|^2 + \|\nabla \operatorname{curl} \mathbf{w}\|^2 \, d\mathbf{x} \quad (18)$$

which enforces a smoothing constraint not on the motion field \mathbf{w} itself but only on its structural components we are interested in. Hence discontinuities in the motion field resulting from sources, sinks and vortexes are not penalized with this regularization term, but only abrupt changes in strength and direction of those components. Replacing \mathbf{w} by its definition (7) (and neglecting the laminar component), this regularization term takes the form

$$\int_{\Omega} \|\nabla \operatorname{div} \nabla \phi\|^2 + \|\nabla \operatorname{curl} \nabla \psi^{\perp}\|^2 \, d\mathbf{x} \quad (19)$$

since $\operatorname{div} \nabla \psi^{\perp} = 0$ and $\operatorname{curl} \nabla \phi = 0$ by definition (see (2), (4-5)). Unfortunately, the high-order derivatives render a direct numerical approach quite involved. To overcome this problem we follow the approach of Corpetti et al. [4] and introduce auxiliary variables ξ_1 and ξ_2 , enforce them to approximate $\operatorname{curl} \nabla \psi^{\perp}$ and $\operatorname{div} \nabla \phi$ by additional (soft) constraints and impose the original regularization constraint on them, i.e.

$$\int_{\Omega} \gamma \left([\operatorname{div} \nabla \phi - \xi_2]^2 + [\operatorname{curl} \nabla \psi^{\perp} - \xi_1]^2 \right) + \lambda \left(\|\nabla \xi_2\|^2 + \|\nabla \xi_1\|^2 \right) \, d\mathbf{x}, \quad (20)$$

with some regularization parameters $\gamma, \lambda \in \mathbb{R}^+$. As a consequence, the degree of derivation is lowered at the cost of slightly weakening the regularization strength.

The final form of the energy thus becomes

$$\begin{aligned}
 J(\phi, \psi, \xi_1, \xi_2) := & \int_{\Omega} [I(\mathbf{x}, t) - I(\mathbf{x} + \nabla\phi + \nabla\psi^\perp, t + \Delta t)]^2 \\
 & + \gamma \left([\operatorname{div}\nabla\phi - \xi_2]^2 + [\operatorname{curl}\nabla\psi^\perp - \xi_1]^2 \right) \\
 & + \lambda (\|\nabla\xi_2\|^2 + \|\nabla\xi_1\|^2) d\mathbf{x},
 \end{aligned} \tag{21}$$

leading to the minimization problem

$$\arg \min_{\phi, \psi, \xi_1, \xi_2} J(\phi, \psi, \xi_1, \xi_2). \tag{22}$$

As before, the data term can be approximated by separate linearizations with respect to $\nabla\psi^\perp$ and $\nabla\phi$ keeping only the involved regularization terms:

$$\begin{aligned}
 J_1(\phi, \psi, \xi_1) := & \int_{\Omega} [\nabla I_\phi^\top \nabla\psi^\perp + \partial I_\phi]^2 + \gamma [\operatorname{curl}(\nabla\psi^\perp) - \xi_1]^2 \\
 & + \lambda \|\nabla\xi_1\|^2 d\mathbf{x}
 \end{aligned} \tag{23}$$

$$J_2(\phi, \psi, \xi_2) := \int_{\Omega} [\nabla I_\psi^\top \nabla\phi + \partial I_\psi]^2 + \gamma [\operatorname{div}(\nabla\phi) - \xi_2]^2 + \lambda \|\nabla\xi_2\|^2 d\mathbf{x}. \tag{24}$$

As a result, we arrive at the regularized version of (22):

$$\begin{cases} \arg \min_{\psi, \xi_1} J_1(\phi, \psi, \xi_1) \\ \arg \min_{\phi, \xi_2} J_2(\phi, \psi, \xi_2) \end{cases}. \tag{25}$$

2.3 Extensions to Multiple Resolutions

The minimization furthermore can be integrated into a coarse-to-fine framework in order to keep the magnitudes of $\nabla\psi^\perp$ and $\nabla\phi$ on each resolution level preferably small, which lowers the error resulting from the data term linearization.

Given the solutions ϕ^{l-1} and ψ^{l-1} from resolution level $l-1$ (starting with $\phi^0 \equiv 0$ and $\psi^0 \equiv 0$) ϕ^l and ψ^l are calculated by

$$(\psi^l, \xi_1^l) = (P\psi^{l-1}, 0) + \arg \min_{\psi, \xi_1} J_1(\phi, P\psi^{l-1}, \psi, \xi_1, \gamma_l, \lambda_l) \tag{26}$$

$$(\phi^l, \xi_2^l) = (P\phi^{l-1}, 0) + \arg \min_{\phi, \xi_2} J_2(P\phi^{l-1}, \phi, \psi, \xi_2, \gamma_l, \lambda_l) \tag{27}$$

with

$$J_1(\phi, \psi_0, \psi, \xi_1, \gamma, \lambda) := \tag{28}$$

$$\int_{\Omega} [\nabla \bar{I}_{\phi}^{\top} \nabla \psi^{\perp} + \partial \bar{I}_{\phi}]^2 + \gamma [\text{curl} \nabla(\psi_0 + \psi)^{\perp} - \xi_1]^2 + \lambda \|\nabla \xi_1\|^2 dx$$

$$J_2(\phi_0, \phi, \psi, \xi_2, \gamma, \lambda) := \tag{29}$$

$$\int_{\Omega} [\nabla \bar{I}_{\psi}^{\top} \nabla \phi + \partial \bar{I}_{\psi}]^2 + \gamma [\text{div} \nabla(\phi_0 + \phi) - \xi_2]^2 + \lambda \|\nabla \xi_2\|^2 dx$$

and

$$\begin{aligned} \bar{I}(\mathbf{x}, t) &:= I(\mathbf{x}, t) \\ \bar{I}(\mathbf{x}, t + \Delta t) &:= I(\mathbf{x} + \nabla \phi_0 + \nabla \psi_0^{\perp}, t + \Delta t). \end{aligned} \tag{30}$$

Let P be a prolongation operator mapping from resolution level $l-1$ to l . Except for the first resolution level ϕ and ψ are incremental refinements of the complete solution. Note that the linearization of the data terms is carried out only for the increments, in order to keep the linearization error small, since solutions from coarser resolutions ($P\phi^{l-1}$ and $P\psi^{l-1}$) are included in the data itself (cf. (30)). (30) is equivalent to an incremental back-mapping of a each frame to its predecessor.

In contrast to that the regularization terms apply to the complete potential functions ($P\phi^{l-1} + \phi$ and $P\psi^{l-1} + \psi$), not only to the increments. For the auxiliary variables the coarse-to-fine method is not applied here, since they are not involved in the linearization. Hence, ξ_1 and ξ_2 are non-increments and calculated independently at each resolution.

2.4 Minimization and Discretization

In order to evaluate (26) and (27), we compute the Euler-Lagrange equations for J_1 w.r.t. ψ, ξ_1 and for J_2 w.r.t. ϕ and ξ_2 :

$$\left\{ \begin{array}{l} \text{curl} \left((\nabla \bar{I}_{\phi}^{\top} \nabla \psi^{\perp} + \partial \bar{I}_{\phi})^{\top} \nabla \bar{I}_{\phi} \right) + \gamma [\Delta^2(\psi_0 + \psi) + \Delta \xi_1] = 0 \\ \gamma [\Delta(\psi_0 + \psi) + \xi_1] - \lambda \Delta \xi_1 = 0 \\ \text{div} \left((\nabla \bar{I}_{\psi}^{\top} \nabla \phi + \partial \bar{I}_{\psi})^{\top} \nabla \bar{I}_{\psi} \right) + \gamma [\Delta^2(\phi_0 + \phi) - \Delta \xi_2] = 0 \\ \gamma [-\Delta(\phi_0 + \phi) + \xi_2] - \lambda \Delta \xi_2 = 0 \end{array} \right. . \tag{31}$$

The Biharmonic Operator

$$\Delta^2 = \partial_{x^4} + 2\partial_{x^2 y^2} + \partial_{y^4} \tag{32}$$

occurring in two equations can be discretized by a standard 13-points-stencil [8]. In addition, we impose the boundary conditions

$$\phi(\mathbf{x}) = \sigma_{\phi}(\mathbf{x}) \quad \wedge \quad \nabla_{\mathbf{n}} \phi(\mathbf{x}) = \rho_{\phi}(\mathbf{x}), \quad \forall \mathbf{x} \in \partial \Omega \tag{33}$$

$$\psi(\mathbf{x}) = \sigma_{\psi}(\mathbf{x}) \quad \wedge \quad \nabla_{\mathbf{n}} \psi(\mathbf{x}) = \rho_{\psi}(\mathbf{x}), \quad \forall \mathbf{x} \in \partial \Omega \tag{34}$$

with boundary functions $\sigma_\phi, \sigma_\psi, \rho_\phi$ and ρ_ψ . $\nabla_{\mathbf{n}}$ denotes the outer normal gradient with respect to Ω .

3 Experimental Results

This section is organized into three parts. First, the quantitative and qualitative influence of the parameters γ and λ is investigated in Section 3.1. Second, the proposed method is compared with the method of Corpetti et al. [5] on artificial motion fields, i.e. with ground truth, in Section 3.2. Finally, results for a real image sequence are presented.

In all experiments, the Euler-Lagrange equations (31) were solved sequentially in 3000 iterations using an incomplete CLG solver iterating 50 times in each (outer) iteration. Two resolution levels (including the original one) have been used for the experiments in Sections 3.1 and 3.2 and three for those in Section 3.3.

Furthermore, due to lack of data, the boundary values of ϕ and ψ have been set to zero, i.e. $\sigma_{\phi,\psi} \equiv 0$. The same has been done for the normal derivatives $\nabla_{\mathbf{n}}\phi, \nabla_{\mathbf{n}}\psi$, i.e. $\rho_{\phi,\psi} \equiv 0$. Since it is not adequate for the vector field to vanish at the border $\partial\Omega$, Ω was artificially enlarged by 30% of the width/height of the original image section and also set to zero¹.

As error measure the *average squared L_2 norm error* and the *average angular error* (mean and first standard derivation) proposed by [10] have been taken. Since the potentials ϕ and ψ are defined up to a constant it was difficult to find an appropriate error measure for the velocity potential and the stream functional directly instead for the derived flow components.

The intensities of all input images have been normalized to $[0, 1]$.

3.1 Parameter Studies

In first experimental studies the influence of the parameters γ and λ were investigated on synthetic potentials in order to have a ground truth (cf. Figure 1). The associated synthetic flow field was applied to a real image, i.e. the real image was mapped using the velocity field to obtain a second image resulting in the input image pair for the current experiments. Note that the vector field consist of an exact spatial overlap of the true components we wish to determine and distinguish.

Figure 3 shows the results for estimation the potential functions with parameter values $\gamma \in \{0.1, 0.25, 0.5, 1, 2, 3, 4\}$ and $\lambda = 10^3$ fixed. These results clearly illustrate the positive regularizing effect of the high-order smoothness terms in (23) and (24) which were made computationally tractable by means of auxiliary functions. It's remarkable that both vector field components can be distinguished — despite a complete spatial overlap and only partially given image structures — by subsequent linearizations of a single data term (cf. Section 2.1).

¹ Note that this is (approximately) consistent with the initial assumption (w.r.t. the Helmholtz Decomposition) that the velocity field vanishes at infinity.

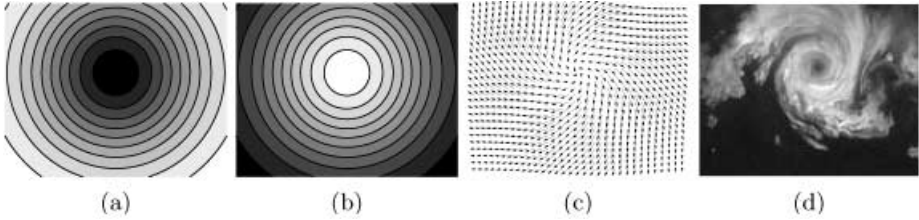


Fig. 1. Setting for Parameters Studies (a) Ground truth velocity potential ϕ (b) Ground truth stream function ψ (c) Associated synthetic velocity field $\mathbf{w} = \nabla\phi + \nabla\psi^\perp$ (d) The real image the velocity field \mathbf{w} was applied to in order to generate the input image pair for the experiments (size: 128×100 pixels). Note that the vector field consist of an exact spatial overlap of the true components we wish to determine and distinguish.

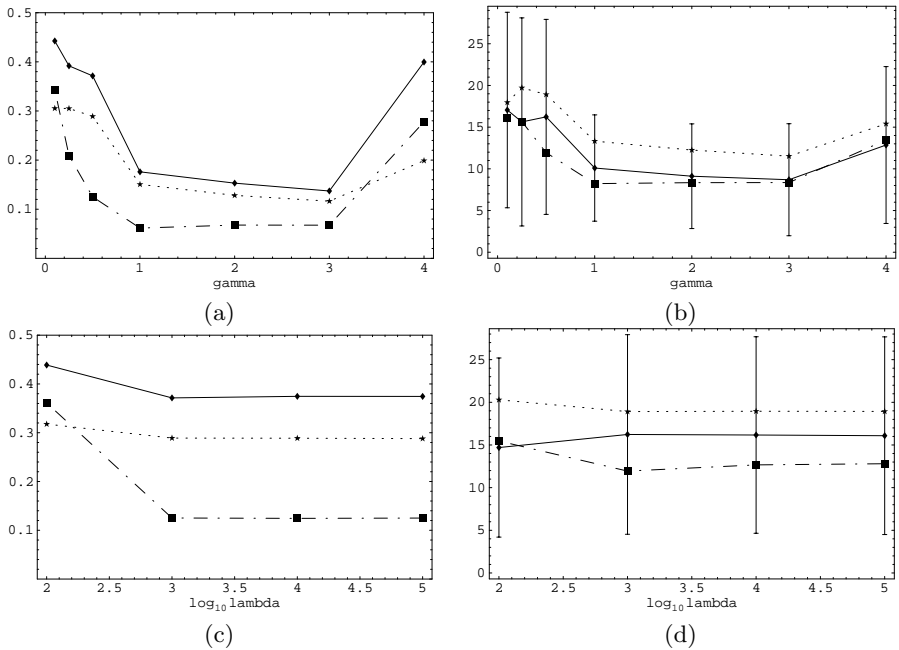


Fig. 2. Influence of parameters λ and γ on error measurements. (a,c) Average squared L_2 norm error of $\hat{\mathbf{w}}_{ir} + \hat{\mathbf{w}}_{so}$ (solid), $\hat{\mathbf{w}}_{ir}$ (pointed) and $\hat{\mathbf{w}}_{so}$ (dashed) depending on γ (a) and λ (c) (b,d) Average angular error of $\hat{\mathbf{w}}_{ir} + \hat{\mathbf{w}}_{so}$ (solid), $\hat{\mathbf{w}}_{ir}$ (pointed) and $\hat{\mathbf{w}}_{so}$ (dashed) depend-ending on γ (b) and λ (d). Direct estimation of potential functions as the objects of primary interest leads to a small global error of the corresponding gradient velocity fields (a,c) but to local angular errors from $10^\circ - 20^\circ$.

Whereas Figs. 2(a,c) and 3(d,k) show that the deformation pattern has been computed well, Figs. 2(b,d) reveal a relatively large angular error of $10^\circ - 20^\circ$ of the respective velocity fields. This is plausible since the velocity fields are related

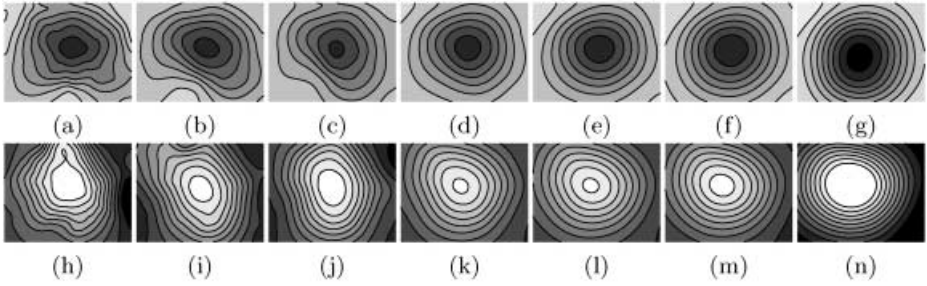


Fig. 3. Qualitative influence of parameter γ . Approximated velocity potentials ϕ (a–g) and stream functions ψ (h–n) for $\gamma \in \{0.1, 0.25, 0.5, 1, 2, 3, 4\}$ and $\lambda = 10^3$. Both vector field components can be distinguished, despite a complete spatial overlap. The positive effect of the high-order regularization implemented by means of auxiliary functions is clearly visible.

to the *derivatives* of the quantities we estimate directly (potential functions). As a consequence, inaccuracies are amplified. However, it should be noted again that the potential functions are the quantities of primary interest for flow pattern analysis. A comparison with an approach which uses *indirect* computation of the potential functions by integrating velocity fields along stream lines is the objective of the next section.

Figure 4 shows that for low values of the regularizing parameter γ the corresponding auxiliary function must not be smoothed too much (too large values of λ). This finding reveals a dependency between γ and λ , the closer investigation of which is left for future work.

3.2 Comparison with the Approaches of Corpetti et al. and Horn and Schunck

In [5] an approach was presented in which the potential functions were approximated *indirectly* by first estimating a motion field using a regularization similar to (21) and a subsequent integration along the stream lines in order to obtain the velocity potential and the stream function. Both approaches were compared in two experiments here based on given synthetic potential functions (cf. Figure 5). In order to have a reference both experiments have been carried out with a Horn and Schunck estimator also. The parameters of all methods have been optimized manually. Note that the setting of Comparison Experiment 1 is the same as for the parameters studies.

The results for Experiment 1 (Figure 6 and Table 1) and Experiment 2 (Figure 7 and Table 2) both show that the new approach yield similar good results as the approach of Corpetti et al., despite the higher order of differential equations involved in the minimization. Furthermore, they show that the standard regularization of Horn and Schunck is insufficient to preserve the desired image structures, since this regularization penalizes strong discontinuities like those in the center of the velocity field in Experiment 1 resulting from a vortex and a

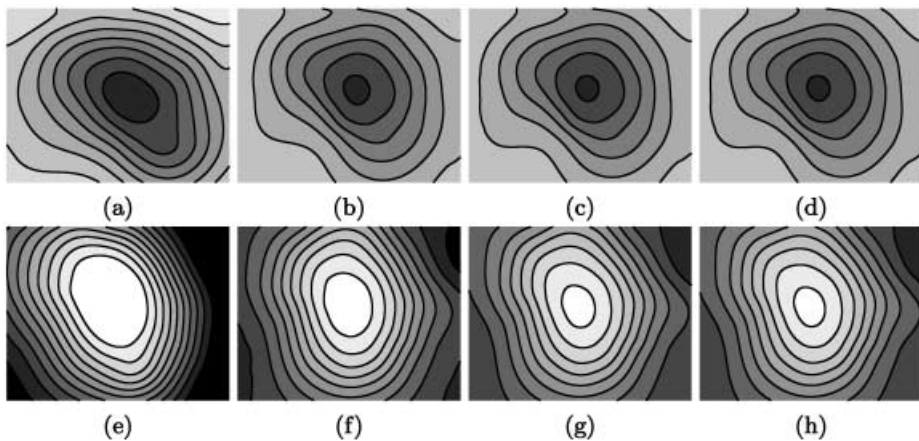


Fig. 4. Qualitative influence of parameter λ . Approximated velocity potentials ϕ (a-d) and stream functions ψ (e-h) for $\lambda \in \{10^2, 10^3, 10^4, 10^5\}$ and $\gamma = 0.5$. Parameters for enforcing regularization γ and smoothing the auxiliary functions λ are not independent. For low values of γ , the auxiliary functions must not be smoothed too much.

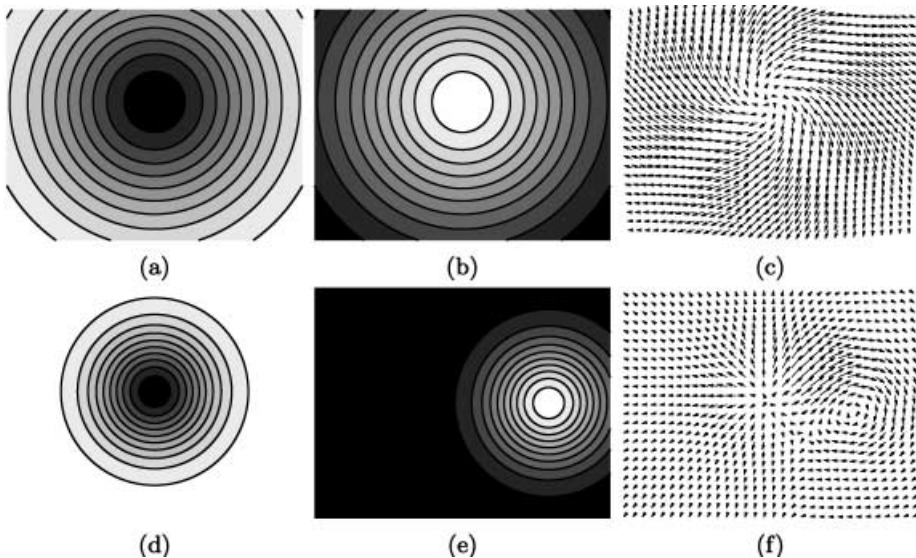


Fig. 5. Setting for Comparison Experiments 1–2. (a,b) Ground truth velocity potential ϕ and stream function ψ for Comparison Experiment 1 (c) Associated velocity field $\mathbf{w} = \nabla\phi + \nabla\psi^\perp$, $\max\|\mathbf{w}\| = 1.86$ (d,e) Ground truth velocity potential ϕ and stream function ψ for Comparison Experiment 2 (f) Associated velocity field $\mathbf{w} = \nabla\phi + \nabla\psi^\perp$, $\max\|\mathbf{w}\| = 1.89$. Both synthetic velocity fields have been used to map the real image in Figure 1(d) in order to generate the second images of the input image pairs.

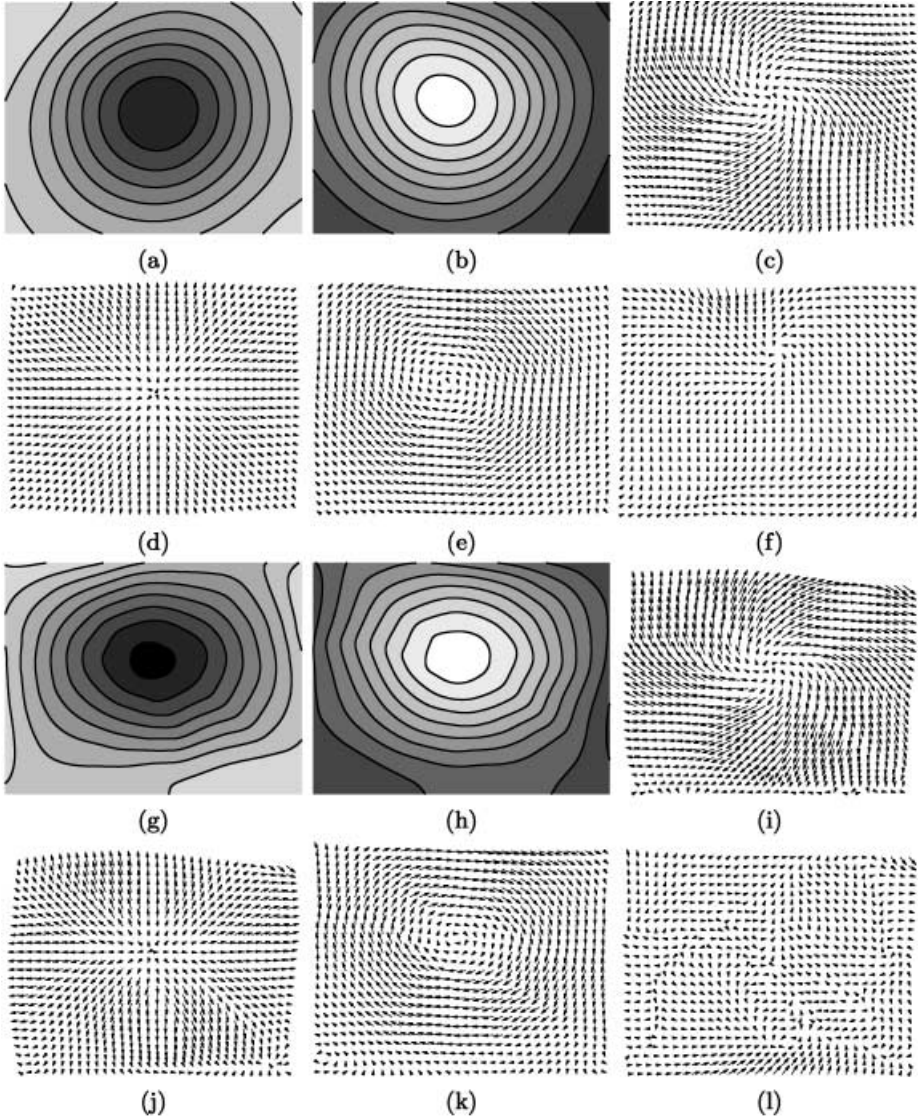


Fig. 6. Results of Comparison Experiment 1. Results of the direct approach ($\gamma = 3.0, \lambda = 1000$): (a) Velocity potential $\hat{\phi}$ (b) Stream function $\hat{\psi}$ (c) Associated velocity field $\hat{\mathbf{w}}$ (d) Irrotational part of the vel. field $\hat{\mathbf{w}}_{ir}$ (e) Solenoidal part of the vel. field $\hat{\mathbf{w}}_{so}$ (f) Difference between approximated and true vel. field $\hat{\mathbf{w}} - \mathbf{w}$. Result of the Corpetti et al. approach ($\alpha = 300, \lambda = 250$): (g) Velocity potential $\hat{\phi}$ (h) Stream function $\hat{\psi}$ (i) Associated velocity field $\hat{\mathbf{w}}$ (j) Irrotational part of the vel. field $\hat{\mathbf{w}}_{ir}$ (k) Solenoidal part of the vel. field $\hat{\mathbf{w}}_{so}$ (l) Difference between approximated and true vel. field $\hat{\mathbf{w}} - \mathbf{w}$. Both methods lead to very similar results in this case, despite significant differences in the approach.

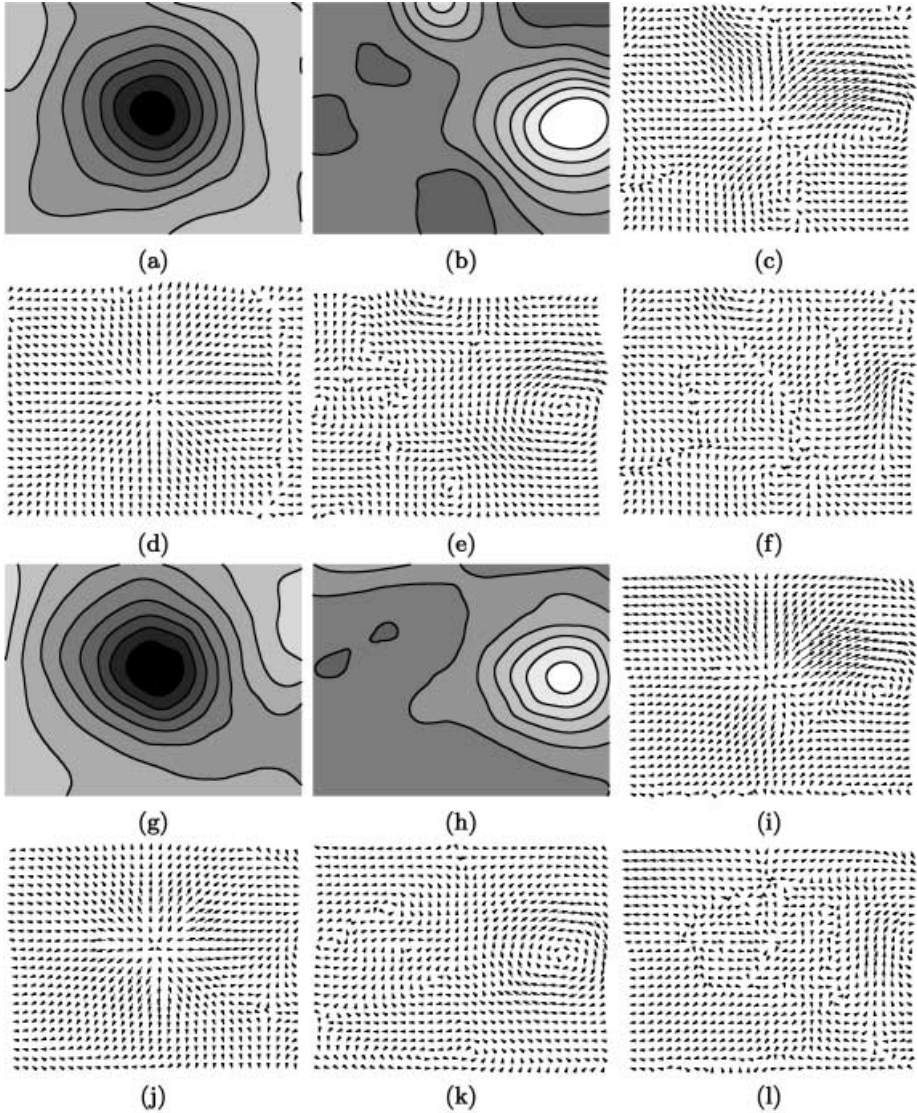


Fig. 7. Results of Comparison Experiment 2. Results of the direct approach ($\gamma = 0.5, \lambda = 100$): (a) Velocity potential $\hat{\phi}$ (b) Stream function $\hat{\psi}$ (c) Associated velocity field $\hat{\mathbf{w}}$ (d) Irrotational part of the vel. field $\hat{\mathbf{w}}_{ir}$ (e) Solenoidal part of the vel. field $\hat{\mathbf{w}}_{so}$ (f) Difference between approximated and true vel. field $\hat{\mathbf{w}} - \mathbf{w}$. Results of the Corpetti et al. approach ($\alpha = 300, \lambda = 250$): (g) Velocity potential $\hat{\phi}$ (h) Stream function $\hat{\psi}$ (i) Associated velocity field $\hat{\mathbf{w}}$ (j) Irrotational part of the vel. field $\hat{\mathbf{w}}_{ir}$ (k) Solenoidal part of the vel. field $\hat{\mathbf{w}}_{so}$ (l) Difference between approximated and true vel. field $\hat{\mathbf{w}} - \mathbf{w}$. Also here the results are quite similar, although the false second maximum of the stream function is more distinct with the direct approach.

Table 1. Approximation errors of Comparison Experiment 1. Both the *average squared L_2 norm error* and the *average angular error* of the complete velocity field ($\mathbf{w}_{ir} + \mathbf{w}_{so}$) as well as for the irrotational and solenoidal components (\mathbf{w}_{ir} , \mathbf{w}_{so}) are depicted. Approach dependent parameters have been optimized manually. The errors of the Horn and Schunck approach show clearly that, despite the flow directions are estimated similarly well, there is a significant higher error in the magnitudes which results from the penalization of the discontinuity in the velocity field (cf. Fig. 5(c)).

Approach/ Error Measure		Direct Approach $\gamma = 3.0, \lambda = 1000$	Corpetti et al. $\alpha = 300, \lambda = 250$	Horn&Schunck $\alpha^2 = 0.17$
Aver. Sq. L_2 Norm Error $\times 10^3$	$\mathbf{w}_{ir} + \mathbf{w}_{so}$	137.11	175.81	208.979
	\mathbf{w}_{ir}	116.38	152.89	
	\mathbf{w}_{so}	67.51	102.24	
Aver. Angular. Error (Mean/1. Stand. Dev.)	$\mathbf{w}_{ir} + \mathbf{w}_{so}$	$8.69^\circ \pm 6.72^\circ$	$10.12^\circ \pm 7.95^\circ$	$8.93^\circ \pm 6.39^\circ$
	\mathbf{w}_{ir}	$11.52^\circ \pm 5.58^\circ$	$12.89^\circ \pm 7.71^\circ$	
	\mathbf{w}_{so}	$8.35^\circ \pm 5.39^\circ$	$10.36^\circ \pm 6.12^\circ$	

Table 2. Approximation errors of Comparison Experiment 2. While the approximation quality compared to the indirect approach of Corpetti et al. is more equal here, the difference in approximation quality to the approach of Horn and Schunck is not as distinct as in Experiment 1 since the discontinuities of the velocity field are smaller in this case see Fig. 5(f)).

Approach/ Error Measure		Direct Approach $\gamma = 0.5, \lambda = 100$	Corpetti et al. $\alpha = 300, \lambda = 250$	Horn&Schunck $\alpha^2 = 0.07$
Aver. Sq. L_2 Norm Error $\times 10^3$	$\mathbf{w}_{ir} + \mathbf{w}_{so}$	162.18	168.7	170.514
	\mathbf{w}_{ir}	60.69	70.59	
	\mathbf{w}_{so}	129.56	65.76	
Aver. Angular. Error (Mean/1. Stand. Dev.)	$\mathbf{w}_{ir} + \mathbf{w}_{so}$	$14.68^\circ \pm 9.59^\circ$	$14.65^\circ \pm 11.51^\circ$	$16.19^\circ \pm 10.26^\circ$
	\mathbf{w}_{ir}	$10.56^\circ \pm 5.93^\circ$	$11.15^\circ \pm 7.52^\circ$	
	\mathbf{w}_{so}	$14.11^\circ \pm 9.72^\circ$	$10.29^\circ \pm 7.36^\circ$	

source, which we want to preserve. Even for weak regularizations the results of the Horn and Schunck estimator is less accurate in both experiments.

3.3 Reconstructing the Vortexes of a Landing Air Plane

Finally, the new approach has been applied on an image pair coming from a real image sequence. The sequence is a recording of the motion of smoke behind a landing passenger air plane. It contains a strong vortex in the center and a weaker but larger one in the other direction with its center laying outside the image plane, approximately 50% from the right border. In addition a weak source is present in the right half, centered vertically (cf. Figure 8(a,b)).

In order to eliminate the laminar component of the velocity field, the laminar flow has been approximated roughly by a Horn and Schunck estimator with a strong regularization $\alpha^2 = 10^6$ and used to map the second image of the input image pair back (cf. Section 2.1).

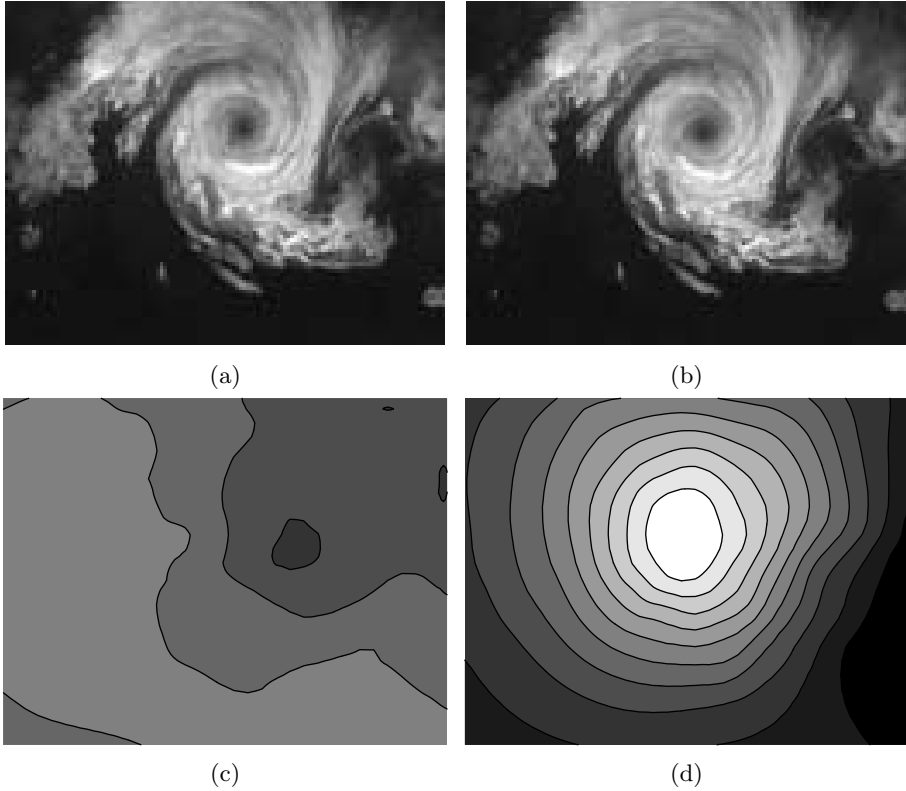


Fig. 8. Result of the Air Plane Sequence Experiment. (a,b) Two successive images from the sequence, gray values, 128×100 pixels (c) Approximated velocity potential $\hat{\phi}$ (d) Approximated stream function $\hat{\psi}$ (e) Associated irrotational component $\hat{\boldsymbol{w}}_{ir}$ (f) Associated solenoidal component $\hat{\boldsymbol{w}}_{so}$. Parameters were: $\gamma = 0.5$, $\lambda = 10^3$, Maximum approximated displacement: $\max \|\hat{\boldsymbol{w}}\| = 2.75$. The image sequence contains a strong vortex in the center and a weaker but larger one in the other direction laying outside, approximately 50% from the right border. In addition a weak source is present in the right half, vertically centered. Both the main vortex and the weak source are well reconstructed despite the lack of image structures in the lower half of the sequence. But the weaker counter-vortex is detected only in outlines. This is plausible since the latter one has its maximum outside the image plane and the velocity potential ψ is set to be zero on the enlarged border.

The results in Figure 8 show that both the main vortex and the weak source are well reconstructed, despite the lack of image structures in the lower half of the sequence. But the weaker counter-vortex is detected only in outlines. This is plausible since the latter one has its maximum outside the image plane and the stream function ψ is set to be zero on the large border (see beginning of this section).

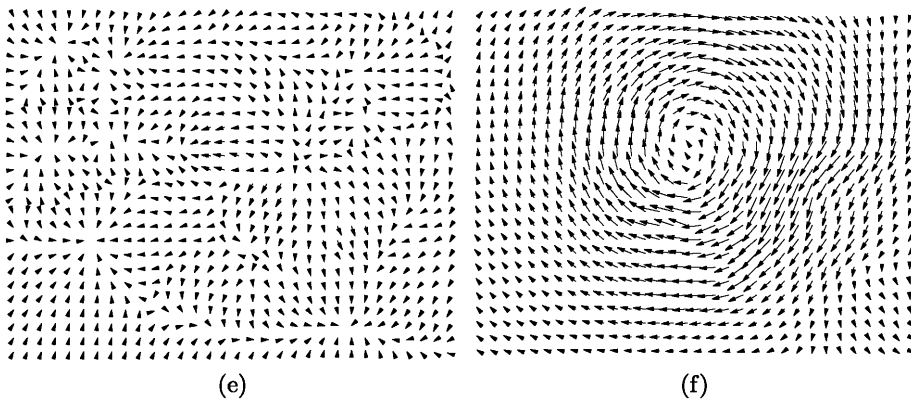


Fig. 8. (Continued).

4 Conclusion

Many important application areas pose the problem of computing highly non-rigid fluid flow from image sequences. In contrast to traditional variational approaches for optical flow computation which are not appropriate in this context, we dealt with this problem by using higher-order regularization terms which merely penalize changes of the principal flow constituents. The approach was made computationally tractable by the use of auxiliary functions. A significant feature of our approach is that the associated potential functions are directly computed. This is a favorable property regarding the recognition and analysis of flow patterns. Numerical experiments confirmed that both components can be estimated separately by subsequent linearizations of a single data term. A comparison with an indirect approach revealed no loss in performance, despite the higher order of differential equations to be solved.

Our further work will focus on the computation of the laminar flow in the same step as well, and on the problem of unknown boundary conditions at the image border (recall that, at present, we use standard boundary conditions for the biharmonic operator at an artificially enlarged image border). Moreover, we will investigate in more detail the dependency on the auxiliary functions and corresponding smoothing terms.

References

1. R. Adrian. Particle imaging techniques for experimental fluid mechanics. *Annal Rev. Fluid Mech.*, 23:261–304, 1991.
2. A. Amini. A scalar function formulation for optical flow. In *Proc. Europ. Conf. Computer Vision*, pages 125–131, 1994.
3. L. Bannehr, R. Rohn, and G. Warnecke. A functional analytic method to derive displacement vector fields from satellite image sequences. *Int. Journ. of Remote Sensing*, 17(2):383–392, 1996.

4. T. Corpetti, E. Mémin, and P. Pérez. Dense estimation of fluid flows. *IEEE Trans. Pattern Anal. Machine Intell.*, 24(3):365–380, 2002.
5. T. Corpetti, E. Mémin, and P. Pérez. Dense motion analysis in fluid imagery. In *European Conference on Computer Vision, ECCV'02*, pages 676–691, 2002.
6. S. Das Peddada and R. McDevitt. Least average residual algorithm (LARA) for tracking the motion of arctic sea ice. *IEEE trans. on Geoscience and Remote sensing*, 34(4):915–926, 1996.
7. J.M. Fitzpatrick and C.A. Pederson. A method for calculating fluid flow in time dependant density images. *Electronic Imaging*, 1:347–352, 1988.
8. W. Hackbusch. *Theorie und Numerik elliptischer Differentialgleichungen*. B.G. Teubner, Stuttgart, 1986.
9. B. Horn and B. Schunck. Determining optical flow. *Artificial Intelligence*, 17:185–203, 1981.
10. D. J. Fleet J. L. Barron and S. S. Beauchemin. Perfomance of optical flow techniques. *Int. J. Computer Vision*, 1994.
11. R. Larsen, K. Conradsen, and B.K. Ersboll. Estimation of dense image flow fields in fluids. *IEEE trans. on Geoscience and Remote sensing*, 36(1):256–264, 1998.
12. S.P. McKenna and W.R. McGillis. Performance of digital image velocimetry processing techniques. *Experiments in Fluids*, 32:106–115, 2002.
13. A. Ottenbacher, M. Tomasini, K. Holmlund, and J. Schmetz. Low-level cloud motion winds from Meteosat high-resolution visible imagery. *Weather and Forecasting*, 12(1):175–184, 1997.
14. C. Schnörr. Segmentation of visual motion by minimizing convex non-quadratic functionals. In *12th Int. Conf. on Pattern Recognition*, Jerusalem, Israel, Oct 9-13 1994.
15. C. Schnörr, R. Sprengel, and B. Neumann. A variational approach to the design of early vision algorithms. *Computing Suppl.*, 11:149–165, 1996.
16. J. Shukla and R. Saha. Computation of non-divergent streamfunction and irrotational velocity potential from the observed winds. *Monthly weather review*, 102:419–425, 1974.
17. J. Simpson and J. Gobat. Robust velocity estimates, stream functions, and simulated Lagrangian drifters from sequential spacecraft data. *IEEE trans. on Geosciences and Remote sensing*, 32(3):479–492, 1994.
18. S.M. Song and R.M. Leahy. Computation of 3D velocity fields from 3D cine and CT images of human heart. *IEEE trans. on medical imaging*, 10(3):295–306, 1991.
19. D. Suter. Motion estimation and vector splines. In *Proc. Conf. Comp. Vision Pattern Rec.*, 1994.
20. J. Weickert and C. Schnörr. A theoretical framework for convex regularizers in pde-based computation of image motion. *Int. J. Computer Vision*, 45(3):245–264, 2001.
21. L. Zhou, C. Kambhamettu, and D. Goldgof. Fluid structure and motion analysis from multi-spectrum 2D cloud images sequences. In *Proc. Conf. Comp. Vision Pattern Rec.*, volume 2, pages 744–751, Hilton Head Island, South Carolina, USA, 2000.